# Computational investigation of variation in wing aerodynamic load under effect of aeroelastic deformations[†]

Ngoc T. B. Hoang[*]

*School of Transportation Engineering, Hanoi University of Science and Technology, Dai Co Viet, Hai Ba Trung, Hanoi, Vietnam*

---

## Abstract

The evaluation of the variation in aerodynamic load on a wing under the effect of elastic deformations requires solving the problem of wing deformation when wings are subjected to distributed aerodynamic load. This paper presents the calculation of coupling the aeroelastic system for 3D wings. The aerodynamic problem was solved by the doublet–source method for 3D wings, with wing thickness considered. The problem of elastic deformation was solved by the finite element method for hollow 3D wings, with beams arranged inside. Results concerning aerodynamic load on the wing were considered input parameters for the calculation concerning the problem of wing deformation, and those about the deformed wing geometry were deemed input parameters for the calculation regarding the problem of wing aerodynamics for the second calculation. The calculations concerning these problems were repeated until the wing twist angle converged. Analyses and comparisons were performed on the distributions of aerodynamic loads on the rigid and deformed wings to examine the change of the aerodynamic load depending on the structure (aerodynamic loads being functions of the external geometry of the wing, the incidence angle, and the velocity at infinity are solutions of the pure aerodynamic problem). Results regarding wing twists and stress distributions for hollow wings with and without beams inside were presented to assess the cause of changes in aerodynamic load and wing static durability. Aeroelastic calculations were formulated with different velocities at infinity to indicate the need for a suitable structural solution when the aerodynamic load is expected to reach a high value.

*Keywords*: Doublet-source method; Aerodynamic load; Finite element method; Beams; Stress; Aeroelasticity; 3D wing

---

## 1. Introduction

The external shape of a wing is designed to meet the criteria of aerodynamic quality. In the subsonic flow range (free Mach number $M_\infty < 0.65$), the aerodynamic profile has a blunt leading edge, and the wing has a large aspect ratio. The airplane wing is considered thin when the wing thickness is significantly smaller than the chord length and wingspan, and thus, the wing is deformed when subjected to large aerodynamic forces, which the wing encounters because of its function of lifting the entire weight of the aircraft. In terms of structure, the wing is required to be lightweight and yet have high firmness and elasticity; therefore, the wing commonly has a hollow structure with internal beams. In the elastic deformation problem, the wing is treated as a hollow bar clumped to the fuselage at the wing root, in relation to which the wing may be bent or twisted. When a deformation causes the wing to twist, the local incidence angle is altered. This variation results in a change in aerodynamic load distribution on the wing, given that the aerodynamic force depends on the incidence angle.

As an industrial product, the wing needs to meet aerodynamic and structural criteria. These two sets of criteria represent highly different fields of mechanics in terms of differential equation systems that describe physical phenomena and solutions to these equation systems. Several studies have attempted to solve the issues of combining aerodynamic and structural criteria. The reliable prediction of physical phenomena likely leads to a reduction in the time and cost of experimentation, fabrication, and testing. Yoon et al. analyzed the effect of control reversal and torsional divergence on a high-aspect-ratio wing by using a two-step process involving a two-dimensional (2D) cross-sectional analysis and a one-dimensional (1D) beam analysis combined with a 2D simple aerodynamic model [1]. To optimize the shape of wind turbine blades in the presence of aeroelastic deformation effect, Yu et al. [2] used a method coupling computational fluid dynamics and computational solid dynamics solvers for the aeroelastic problem of solid wings. Sectional shape optimization based on 2D calculation can lead to non-uniform wings threaded from sections (profiles). To receive static aeroelastic responses, a previous work [3] constructed an aeroelastic coupling between the vortex lattice method (for calculating aerodynamics of

potential flows on the lift surface of wings without wing thickness) and the finite element method (FEM; for computing deformations of a straight wing with an airfoil cross section modeled as a clamped beam). To study the optimum wing shape of a highly flexible morphing aircraft, a study [4] used a coupling of two calculations of wing deformation and aerodynamics. The wing was considered to be a strain-based geometrically nonlinear solid beam, and a study of unsteady aerodynamic loads based on the 2D finite-state inflow was used in the aerodynamic problem. Aeroelastic calculations typically focus on solving the elasticity problem, whereas fixed values are used for aerodynamic forces or are solved using simple methods.

The current research is also geared toward programming codes for solving the aerodynamic and structural problems. The aerodynamic code implementing the doublet–source method (DSM) can obtain the characteristics of a potential subsonic flow for 3D wings (rectangular and trapezoidal) accounting for wing thickness [5]. The structural code using FEM can determine the structure responses for hollow 3D wings with beams and ribs inside.

For analyzing structural and flow problems of ultralight aircraft wings, an article [6] applied the commercial software ANSYS Fluent to wings with spars and ribs. The use of ANSYS Fluent can solve dynamic aeroelastic problems [7]. Other methods for coupling aeroelastic systems adopt such commercial software as FLUENT-ABAQUS [8] and FLUENT-MSC/NASTRAN [9-11]. In general, commercial software are multifunctional and can solve a wide range of problems due to their capability to cover several systems of differential equations and boundary conditions. These software thus require a large memory capacity and long running time. Meanwhile, changing input parameters is often time consuming and thus cannot be performed automatically, thereby leading to the redrawing of the geometry and rebuilding of the grid. In addition, proper meshing requires experience in handling numerical data and knowledge of physics. Physical results must be compared to verify the steps in running a software. With the development of a professional computer program for coupling DSM and FEM, the running time, memory capacity, possibility to change the grid, and input parameters automatically are improved within certain definitions of research.

## 2. Aerodynamic problem

### 2.1 Mathematical formulation and numerical method

Distributed doublets and sources on wing surface elements were used for the aerodynamic problem in this work. This singularity method can solve the flow around a 3D wing while considering the latter's thickness. The upper and lower surfaces of the wing are divided into panels, and each panel (area A) has a source of constant distributed strength s and a doublet of constant distributed strength $\mu$, as shown in Fig. 1(a). The induced velocity potential $\varphi$ at an arbitrary point P(x,y,z) is
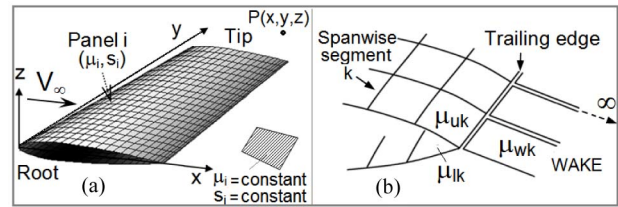


Fig. 1. (a) Wing surface grid; (b) doublet strength of trailing edge upper and lower panel and corresponding wake doublet strength.

the sum of the velocity potentials induced from the doublet $\varphi_D$ and the source $\varphi_S$. The velocity potentials $\varphi_D$ and $\varphi_S$ are determined by the following formulas [12]:

$$\varphi_S(x,y,z) = \frac{-s}{4\pi} \int_A \frac{dA}{\sqrt{(x-x_0)^2 + (y-y_0)^2 + z^2}} , \qquad (1)$$

$$\varphi_D(x,y,z) = \frac{-\mu}{4\pi} \int_A \frac{z\,dA}{\left[(x-x_0)^2 + (y-y_0)^2 + z^2\right]^{3/2}} . \qquad (2)$$

The velocity components (u, v, w) induced from the singularities of the source and the doublet are determined from the derivatives of the velocity potential $\varphi$.

$$(u,v,w) = (\partial\varphi/\partial x, \partial\varphi/\partial y, \partial\varphi/\partial z) . \qquad (3)$$

The velocity components u and v are continuing at any point, but the normal velocity component w is discontinuing when z→0: $w_S(z = 0\pm) = \pm s/2$; $w_D(z = 0\pm) = \pm\mu/2$. The problem uses the Dirichlet conditions for the internal potential $\varphi_i$: $\varphi_i = (\varphi+\varphi_\infty)_i = $ const. The numbers of points discretized on the profile contour and wingspan are n and m, respectively; N = n×m sliding conditions and m Joukowski conditions are present at the trailing edge. We obtain (n+1)×m equations with (n+1)×m doublet unknowns of vector $\boldsymbol{\mu}$.

$$\boldsymbol{A\mu} = -\boldsymbol{Bs} , \qquad (4)$$

where **A** and **B** are square matrices with elements $a_{ij}$ and $b_{ij}$ being coefficients of influence from doublets and sources.

$$\begin{aligned} a_{ij} &= \varphi_D(\mu_j = 1, x_i, y_i, z_i, x_j, y_j, z_j) \\ b_{ij} &= \varphi_S(s_j = 1, x_i, y_i, z_i, x_j, y_j, z_j) \end{aligned} \quad \text{with } i,j = 1 \div (n \times m), \qquad (5)$$

and **s** denotes a vector of (n×m) sources $\boldsymbol{s = n.q_\infty}$ ($\boldsymbol{q_\infty}$ indicates the dynamic pressure.). The conditions at the trailing edge are as follows:

$$(\mu_{uk} - \mu_{lk}) + \mu_{wk} = 0 \quad \text{with} \quad k = 1 \div m , \qquad (6)$$

where $\mu_u$ and $\mu_l$ represent the upper and lower panel doublet strengths at the trailing edge, respectively, and $\mu_w$ is the constant strength wake doublet element (Fig. 1(b)).

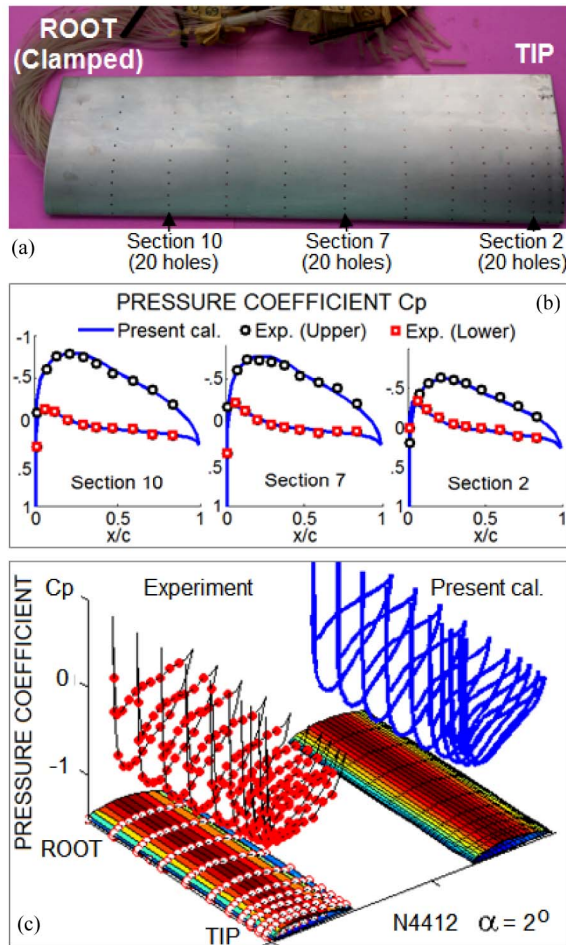The solution of Eq. (4) determines doublets $\boldsymbol{\mu}$ and hence ve-

Fig. 2. (a) Wing model with rows of holes; (b) pressure coefficients on three sections: 10, 7 and 2; (c) 3D representation of pressure coefficients on 10 sections (10 rows of holes).

locities, pressures, and load (from differences of pressures on the lower and upper surfaces of the wing).

### 2.2 Experiment results and validation of program

Experiments were performed to measure the pressure distribution on 3D wings in an open-return wind tunnel with the test section dimension (400 mm × 500 mm) and thus validate the built code. Flow velocities in a wind tunnel with M ≤ 0.15 were created by an exhaust axial fan. Static pressures on the wing surface were measured using a high-quality digital manometer (tolerance: ±0.15 % of full scale ±1digit = (±3±1) Pa).

Wings used in the experiment were rectangular and had the profiles NACA 4412 and NACA 0012 (half of the wingspan was 300 mm, and the chord length was 100 mm.). To avoid disturbance of the flow around the wing, all flexible tubes connecting the gage holes with the digital manometer were completely arranged in the wing. Thus, the wing should be processed within the hollow. A total of 240 holes (in 12 rows, as shown in Fig. 2(a)) with 0.4 mm diameter were drilled on the upper and lower surfaces of the wing (with a wing-half

clamped into the test chamber at the wing root). The wings were constructed from Dural and processed using a CNC milling machine, and pressure gage holes were treated using a CNC–EDM machine (electrical discharge machine). For each pressure measurement value, the number of sampling times was set as 30000 to reduce the random error. With precision in the machining of the model wing and use of high-accuracy measuring devices (digital manometer and Pitot tube), the results of pressure measurement were highly accurate. Experimental results for the NACA 0012 3D wing are shown in Ref. [13]. This paper presents only experimental results obtained under incidence angle α = 2° for the NACA 4412 3D wing and a comparison between the experimental and numerical results of the built aerodynamic code. Fig. 2 presents the pressure coefficient $C_p$, which is determined as follows:

$$C_p = \frac{p - p_\infty}{0.5\rho V_\infty^2} , \qquad (7)$$

where $\rho$ is the air density (at T = 30 °C, $\rho$ = 1.14 kg/m³) and $V_\infty$ denotes the velocity in the wind tunnel. The difference of pressures $p - p_\infty$ was shown on the digital manometer and computer screens ($p$ and $p_\infty$ represent the pressures at the gage hole and were obtained by the Pitot tube.).

Fig. 2 compares the present experimental and numerical results regarding the pressure coefficients distributed on a wing-half with the incidence angle α = 2°. The experimental and numerical results have considerably small differences. Fig. 3 presents the lift coefficients depending on the incidence angle for the NACA 4412 3D wing, with a comparison of numerical results from the present 3D code, the present 3D experimental results, numerical results from 3D viscous Fluent (For verification of the running steps of the software, see Ref. [14].), Pinkerton's 2D experimental results [15], and 2D numerical results from the full potential equation (FPE) code [14]. The FPE code was programmed by the solution of the FPE (and the code solving Euler's equations) to calculate the characteristics of transonic and subsonic flows [14].

Fig. 3 shows that with incidence angles α ≤ 12°, the lift coefficients of the present 3D code, 3D experiments, and 3D viscous Fluent are similar. For incidence angles α > 12°, lift coefficients calculated by potential flow equations (inviscid flow) and real flow equations (viscous flow) are different due to the separation phenomenon of flow. Thus, with incidence angles that are not excessively large (α ≤ 12°) and Mach numbers $M_\infty$ < 0.65, the present 3D aerodynamic code ensures the required accuracy. Fig. 3 also illustrates a large difference between the results for the 3D wing and the 2D profile, particularly when the wing aspect ratio is small.

## 3. Elastic deformation problem

### 3.1 Mathematical formulation and numerical method

The equilibrium equations of a solid determine the relationship between stress and external force. The relationship be-
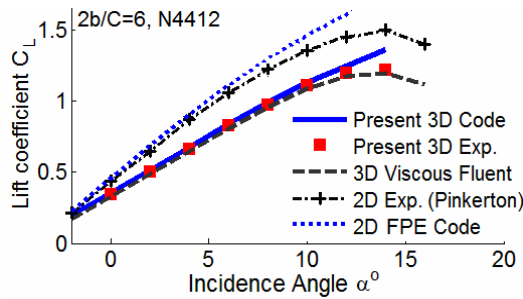
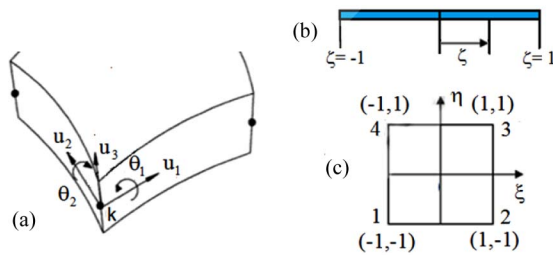Fig. 3. Lift coefficient depending on incidence angle.



Fig. 4. (a) Degrees of freedom at k; (b) 1D shape function H($\zeta$); (c) 2D shape function N($\xi,\eta$).

tween stress and strain is written as follows [16]:

$$\sigma = D\varepsilon \,, \tag{8}$$

where $\sigma$ is the stress vector: $\sigma = [\sigma_x \ \sigma_y \ \sigma_z \ \tau_{xy} \ \tau_{yz} \ \tau_{zx}]^T$. $D$ indicates a matrix of material characteristics depending on the modulus of elasticity E and the Poisson coefficient $\upsilon$. $\varepsilon$ represents the strain vector $\varepsilon = [\varepsilon_x \ \varepsilon_y \ \varepsilon_z \ \gamma_{xy} \ \gamma_{yz} \ \gamma_{zx}]^T$. The relationship between the displacement and strain is as follows:

$$\varepsilon = \partial u \,, \tag{9}$$

where $u$ denotes the displacement vector: $u = [u \ v \ w]^T$. Normal strains are $\varepsilon_x = \partial u/\partial x$, $\varepsilon_y = \partial v/\partial y$ and $\varepsilon_z = \partial w/\partial z$. Shear strains include $\gamma_{xy} = \partial u/\partial y + \partial v/\partial x$, $\gamma_{xz} = \partial w/\partial x + \partial u/\partial z$ and $\gamma_{yz} = \partial w/\partial y + \partial v/\partial z$.

To solve the elasticity problem, the principle of minimum total potential energy is applied. The total potential energy $\Pi$ is presented as follows:

$$\Pi = \frac{1}{2}\int_V \sigma^T \varepsilon dV - \int_V u^T f_v dV - \int_S u^T f_s dS - \sum_{i=1}^n u_i^T f_i \,, \tag{10}$$

where $f_i$ is the point force at the node i with the displacement $u_i$; $f_v$ and $f_s$ refer to the vectors of volume and area forces, respectively; and V and S represent the volume and cross-sectional area of the object, respectively.

Wings were discretized into hexahedral elements and approximated by FEM. The wing was a hollow tube structure with a thin shell thickness, so a reduction by a degree of freedom (from 6 DoF to 5 DoF at each node) was feasible (Fig. 4(a)).

In the degenerate 3D model, the displacement vector definition at node k of the discrete element is as follows:

$$q^k = [u_1 \ u_2 \ u_3 \ \theta_1 \ \theta_2] \,. \tag{11}$$

2D shape function N($\xi,\eta$) and 1D shape function H($\xi$) were used to define the coordinate system ($\xi,\eta,\zeta$) that describes the parameters in each point (Figs. 4(b) and (c)). Shape functions $N^k$ and $H^k$ are as follows:

$$N_1 = (1-\xi)(1-\eta)/4 \,; \quad N_2 = (1+\xi)(1-\eta)/4 \,;$$
$$N_3 = (1+\xi)(1+\eta)/4 \,; \quad N_4 = (1-\xi)(1+\eta)/4 \,, \tag{12}$$

$$H^k = [(1+\zeta)(1-\zeta^*) - (1-\zeta)(1+\zeta^*)] \ \| (x_i^k)^t - (x_i^k)^b \| /4 \,, \tag{13}$$

where $\zeta^*$ indicates the position of the reference of the surface and is valued from −1 to 1; $\zeta^* = 0$ denotes the mid-surface; indices t and b stand for the upper and lower surfaces of the shell, respectively; and i = 1,2,3. The position at k is represented by using shape functions.

$$x_i(\xi,\eta,\zeta) = \sum_{k=1}^n N^k(\xi,\eta)x_i^k + \sum_{k=1}^n N^k(\xi,\eta)H^k(\zeta)V_{3i}^k \tag{14}$$

with the unit vector $V_{3i}^k = [(x_i^k)^t - (x_i^k)^b]/\|(x_i^k)^t - (x_i^k)^b\|$.

Displacements at k are as follows:

$$u_i = \sum_{k=1}^n N^k(\xi,\eta)u_i^k + \sum_{k=1}^n N^k(\xi,\eta)H^k(\zeta)(-V_{2i}^k\theta_1^k + V_{1i}^k\theta_2^k) \,. \tag{15}$$

The relationship between displacements $q$ and deformations are as follows:

$$\varepsilon = Bq \,, \tag{16}$$

where $B$ is a matrix that transforms the degrees of freedom via the shape function.

By considering the discrete element e, the potential energy of deformation of the element is as follows ($V_e$ is the volume of the element.):

$$U_e = 0.5\int \sigma_e^T \varepsilon_e dV_e \,. \tag{17}$$

The stiffness matrix of the element is defined as

$$K_e = \int B_e^T D B_e dV_e \,. \tag{18}$$

Then,

$$U_e = 0.5 q_e^T K_e q_e \,, \tag{19}$$
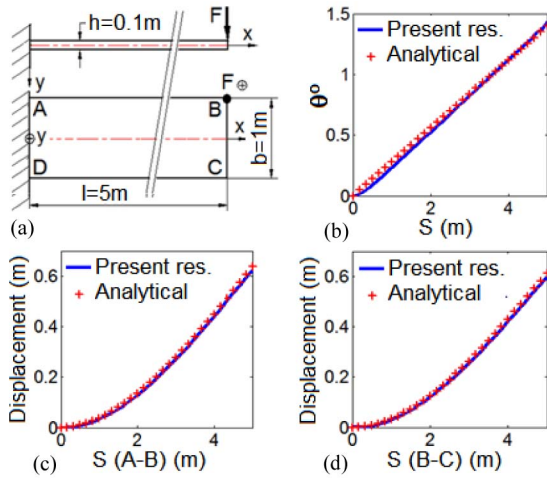
and the total potential energy is defined as follows:

Fig. 5. Twist angles (θ) and displacements.



Fig. 6. Displacements of wing leading and trailing edges subjected to torque and point force (comparison of results).

$$\Pi = \frac{1}{2} \boldsymbol{q}_e^T \boldsymbol{K}_e \boldsymbol{q}_e - \boldsymbol{q}_e^T \boldsymbol{f}_e , \tag{20}$$

where $\boldsymbol{f}_e$ is the node force vector of the element. The principle of minimum total potential energy $\partial \Pi / \partial q = 0$ was applied, and matrix transplantation was performed for matrices $\boldsymbol{K}_e$ and $\boldsymbol{f}_e$ to determine the displacement $\boldsymbol{q}$ and stress $\boldsymbol{\sigma}$. The stress in each element is determined by the von Mises standard.

$$\sigma_{Von-Mises} = \sqrt{\frac{(\sigma_x - \sigma_y)^2 + (\sigma_y - \sigma_z)^2 + (\sigma_x - \sigma_z)^2 + 6(\tau_{yz}^2 + \tau_{zx}^2 + \tau_{xy}^2)}{2}} . \tag{21}$$

### 3.2 Comparison of results and validation of program

Fig. 5(a) shows a rectangular plate that is clamped at the left end. A force $F = 10^5$ N acts at point B. This force is equivalent to the force F located at the midpoint of the segment BC and a moment $M_x = bF/2$. The plate material has a modulus of elasticity (Young's modulus) $E = 8.10^{10}$ N/m$^2$ and Poisson's ratio $\upsilon = 0.3$. The displacement y(x) and twist angle α(x) of this plate are defined as follows:

$$y(x) = -\frac{Fl}{6EJ_y} x^2 \left(3 - \frac{x}{l}\right); \quad \alpha(x) = \frac{M_x}{G\beta \text{bh}^3} x , \tag{22}$$

where $J_y = b^3h/12$ is the second moment of the area, G denotes the shear module $G = 0.5E/(1+\upsilon)$ and $\beta = 0.333$ (with b/h = 10). Displacements of segments AB and CD are y(x)$_{AB}$ = y(x)+0.5bsinα(x) and y(x)$_{CD}$ = y(x)–0.5bsinα(x), respectively. Figs. 5(b)-(d) present the results of the calculation of twist angles and displacements of the plate performed using the analytical formulas and the built code. The analytical and numerical findings are similar, with differences being 1.63 % and 1.81 % for the maximum displacements at B and C, respectively, and 2.71 % for the maximum twist angle.
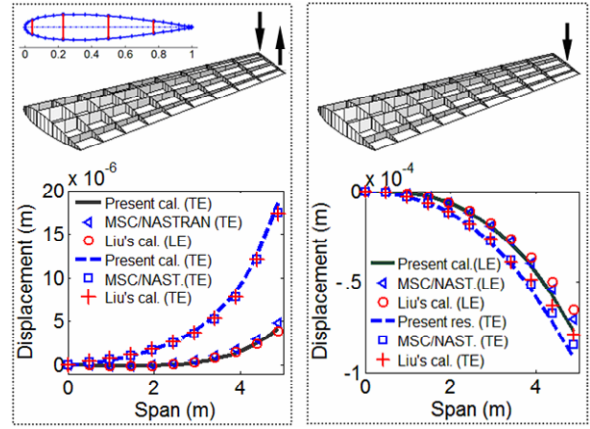
The present structural code (for 3D hollow wings) was used to calculate a problem posed by Liu [17] (Fig. 6). Liu performed calculations of the wing structure subjected to a point force and a torque using FEM and MSC/NASTRAN. Liu's model wing has the following parameters: trapezoidal wing with wingspan of 192 in; 4 beams and 10 ribs distributed evenly; root chord $c_r = 72$ in; tip chord $c_t = 36$ in; NACA 0015 and NACA 0006 root and tip profiles, respectively; skin thickness $t_1 = 0.118$ in; flange thickness $t_2 = 0.197$ in; web thickness $t_3 = t_2$; rib thickness $t_4 = 0.058$ in; flange width $t_5 = 0.373$ in; $E = 1025.10^4$ lb/in$^2$; and $\upsilon = 0.3$. The wing was subjected to two forces: one torque F = 1 lbf at the ends of beams 1 and 4 and one point force F = 1 lbf at the end of beam 3 (Fig. 6). The figure also shows the results on displacements of the leading and trailing edges, with a comparison between the results calculated from the present code and Liu's results calculated by FEM and MSC/NASTRAN. Similar results with differences of less than 5 % were indicated for the methods. An evaluation of the difference in displacement of the leading and trailing edges revealed a significant wing twisting caused by the cases of point force and torque. However, in Liu's work, specialized research was conducted on the wing dynamic structure; hence, no question concerning wing aerodynamic properties was raised.

## 4. Results and discussion

The grid generation of the aerodynamic and structure problems is different. Therefore, aerodynamic load interpolation must be performed from the aerodynamic mesh to the structure mesh. Fig. 7 presents a diagram of the DSM–FEM coupling procedure.

### 4.1 Distribution of pressure and lift coefficients

An assessment was performed on a rectangular wing with span-half b = 5 C, profile NACA 0012, C = 1 m, and incidence angle α = 4°. In terms of aerodynamics, the variable
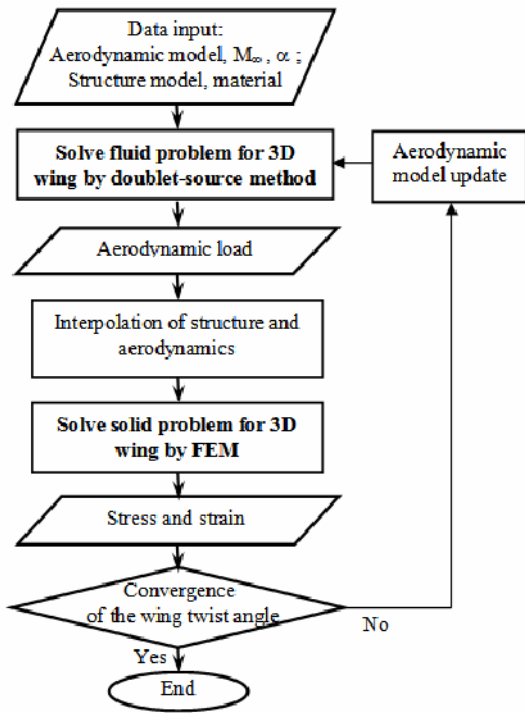
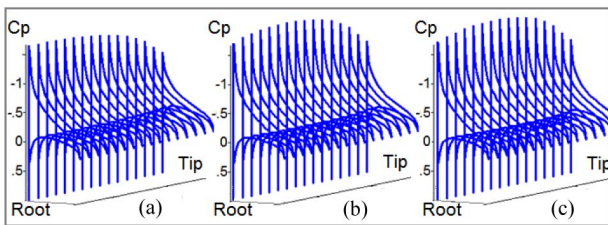Fig. 7. Diagram of DSM–FEM coupling procedure.



Fig. 8. 3D distribution of pressure coefficients on wing-half: (a) Rigid wing; (b) flexible wing (2nd iteration); (c) flexible wing (3rd iteration).
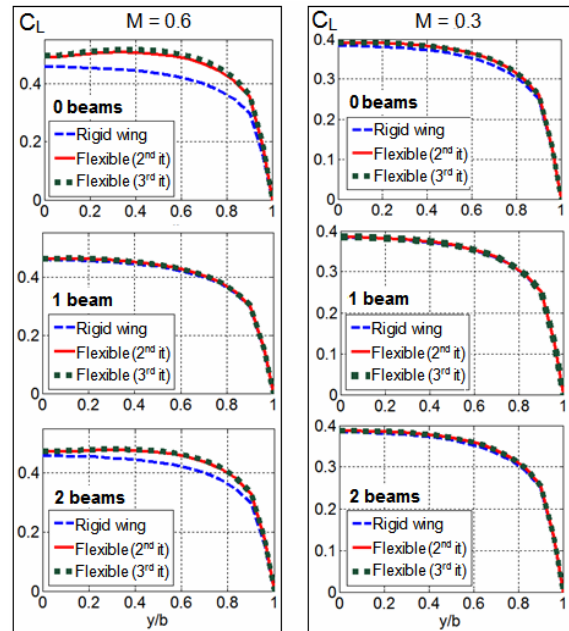


Fig. 9. Lift coefficients on wing-half ($M_\infty = 0.6$, $M_\infty = 0.3$ – wings without beams, with one beam, and with two beams).
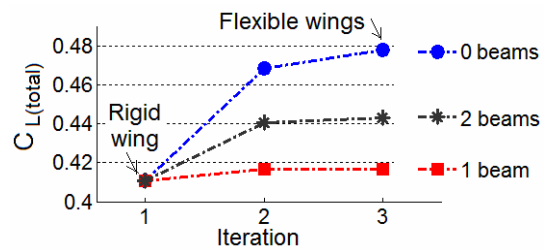


Fig. 10. Total lift coefficients for rigid and flexible wings (without beams, with one beam, with two beams, and $M_\infty = 0.6$).

parameter was the free Mach number ($M_\infty = 0.3$ and $M_\infty = 0.6$). Regarding the wing structure, the variable factor was the number of beams arranged inside the hollow wing.

Fig. 8 shows the 3D distribution of pressure coefficients on the wing for the case of the hollow wing without beams and $M_\infty = 0.6$. The calculation of aeroelastic coupling was repeated three times. In the first calculation (Fig. 8(a)), the distribution of the pressure coefficient on the rigid wing (i.e., the solution of the pure aerodynamic problem) was obtained. Fig. 8(b) presents the wing pressure coefficient distribution when the wing was considered to be rigid and deformed due to the effect of aerodynamic loads. Fig. 8(c) illustrates the pressure coefficient distribution for the deformed wing obtained from the third calculation.

The differences between the results of the second and third calculations were small enough, and thus, the result of the third calculation (Fig. 8(c)) was selected as the solution to the problem concerning the elastic deformation effect of the wing. Large differences were observed in the values and the law of

pressure distributions between the rigid and deformed wings. These differences are also indicated in Fig. 9, showing the lift coefficients for the case of $M_\infty = 0.6$ and wing without beams. Specifically, the lift coefficients were considerably larger for the deformed wing than the rigid wing.

The lift coefficients on a wing-half, presented in Fig. 9, indicated that the lift coefficients in the cases where $M_\infty = 0.6$ were higher than in the cases where $M_\infty = 0.3$ and were thus deformed more than were the latter. In the three cases where the hollow wing had no beam, one beam, and two beams, the lift coefficients of the wings with one beam were nearly unchanged because the wings were almost untwisted. The wings with two beams had larger wing twist angles than the wings with one beam. However, the stress was smaller for the wings with two beams than the wings without beams and with one beam. The total lift coefficients presented in Fig. 10 show the variations in lift when the wing was considered to be rigid or flexible (with the internal structure without beams, with one and two beams, and $M_\infty = 0.6$).
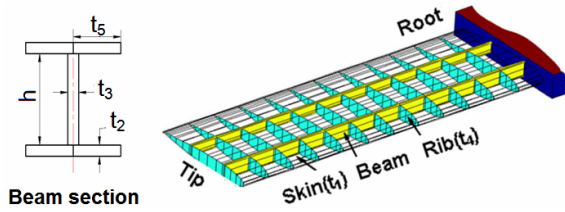
Fig. 11. Definitions of beams, ribs, and skin.

### 4.2 Twist angle of wing

The wing with the aerodynamic parameters described in Sec. 4.1 (b/C = 5, C = 1 m, NACA 0012, and α = 4°) were considered, and wing weights were ignored. The structural parameters of the wing were as follows: Skin thickness $t_1$ = 0.002 m; flange thickness $t_2$ = 0.01 m; web thickness $t_3$ = 0.01 m; rib thickness $t_4$ = 0.008 m; flange width $t_5$ = 0.02 C; depth h determined by beam position (Fig. 11), E = $7.10^{10}$ N/m², υ = 0.33; and allowable stress (based on yield strength) $\sigma_{allow}$ = $14.10^7$ N/m² [18, 19]. Two beams (or one beam) and 15 ribs were distributed evenly. The positions of beams 1 and 2 were 25 % C and 65 % C, respectively, from the leading edge.

Fig. 12 shows the results of wing twist angles when $M_\infty$ = 0.6 and $M_\infty$ = 0.3 in three structural cases: without beams, with one beam, and with two beams. With $M_\infty$ = 0.6, the wing twist angles were remarkably large (up to approximately 1° at the wing tip for the wing without beams). With $M_\infty$ = 0.3 and wing without beams, the maximum twist angle was 0.18°. However, in both cases ($M_\infty$ = 0.6 and $M_\infty$ = 0.3), for the wings with one beam, the wing twist was remarkably small. This result agreed with the theory of the divergence speed on the basis of the 2D hypothesis of the model section in that with the wing with one beam at 25 % C, the distance between the aerodynamic and twist centers was equal to zero. Hence, the wing structure was safe on the torsion divergence, i.e., the wing was stable at all speeds [1, 16].

The wing twist angle was larger for the wing with two beams than that for the wing with one beam. However, increasing the number of beams reduced wing bending and thus also minimized the stress intensity on the wing. This case is analyzed in Sec. 4.3.

### 4.3 Stress distribution

Fig. 13 presents the results from the third calculation with $M_\infty$ = 0.6 for the bending and stress distribution on the wing upper surface for the wings without beams and with two beams. The bending and maximum stress of the wing with two beams were significantly smaller than those of the wing without beams. The maximum stress was found in the root section of the wing.

Fig. 14 shows the stress distributions on the upper and lower sides of the wing root section for the rigid and flexible wings ($M_\infty$ = 0.6). Remarkably high values of the maximum stresses (on upper and lower sides) were seen for the wing without beams. The maximum stress of the deformed wing
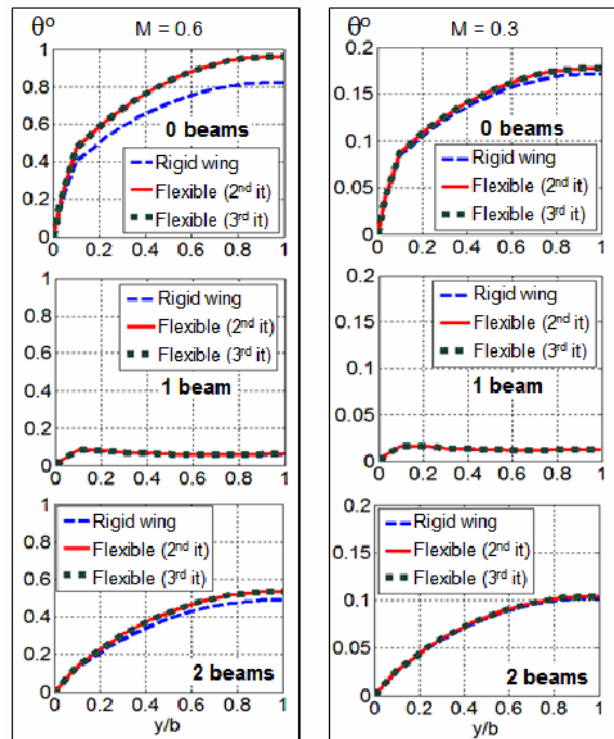


Fig. 12. Twist angles on wingspan-half ($M_\infty$ = 0.6 and $M_\infty$ = 0.3 – wings without beams, with one beam, and with two beams).
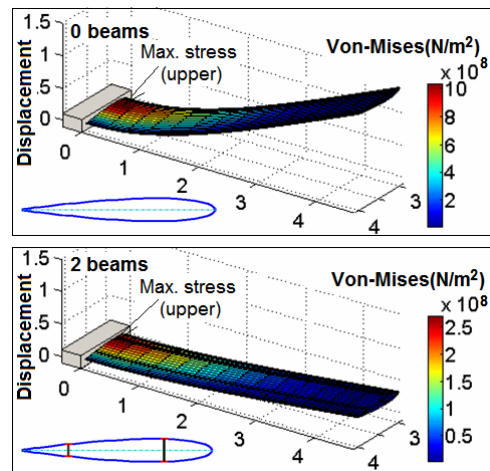


Fig. 13. Displacement and maximal stress on upper surface of flexible wings without beams and with two beams ($M_\infty$ = 0.6).

increased by more than 20 % compared with that of the rigid wing. For the wings with two beams, the maximum stresses reduced by four times compared with those of the wing without beams. In addition, highly similar stresses were observed for the rigid and flexible wings. As shown in Fig. 14, local plastic deformations with respect to the allowable stress could be observed in several places when maximum stress was $M_\infty$ = 0.6. Therefore, with the wing structure in this assessment, $M_\infty$ = 0.6 was inappropriate. For $M_\infty$ = 0.3, a substantial reduction in the maximum stress was observed, as indicated in Fig. 15.
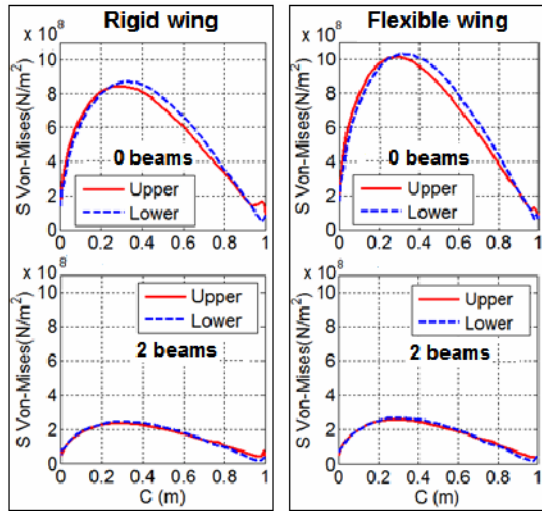
Fig. 14. von Mises stresses in root section of wings without beams and with two beams (rigid and flexible wings, $M_\infty = 0.6$).
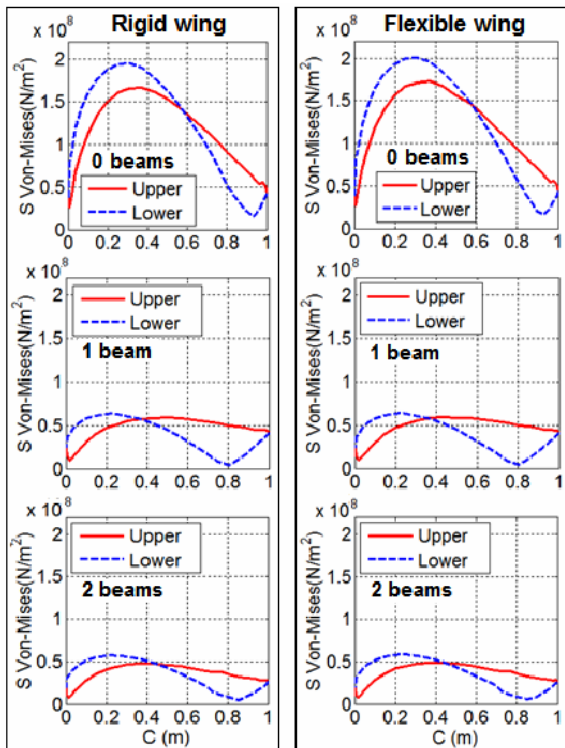


Fig. 15. von Mises stresses in root section of wings without beams, with one beam, and with two beams (rigid and flexible wings, $M_\infty = 0.3$).

### 4.4 Total lift coefficient and maximum stress

The stress distribution on the wing root profile in Fig. 15 shows that at $M_\infty = 0.3$, for the wing with one or two beams, the stresses of the wings before and after deformation remained within the elastic limit. As the velocity changed, the law of stress distribution and maximum stress position on the upper and lower wing surfaces varied considerably. Fig. 16
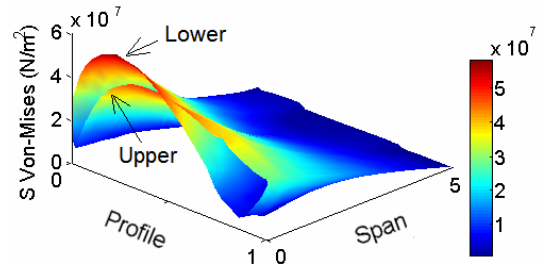


Fig. 16. von Mises stress distribution (3D) on upper and lower surfaces of flexible wing with two beams ($M_\infty = 0.3$).
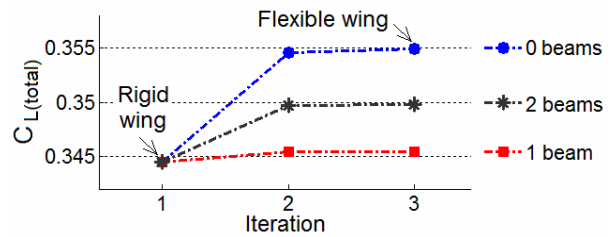


Fig. 17. Total lift coefficients for rigid and flexible wings (without beams, with one beam, and with two beams, $M_\infty = 0.3$).

shows the 3D distribution of stresses on the flexible wing with two beams at $M_\infty = 0.3$. Fig. 17 presents the total lift coefficients when $M_\infty = 0.3$. In the case of rigid wings, the same total lift value was obtained for the wings without beams, with one beam, and with two beams. The number of beams influenced only the total lift coefficient for the flexible wings.

A qualitative similarity was observed between the results shown in Fig. 17 and the results for the total lift coefficient at $M_\infty = 0.6$ in Fig. 10. That is, when the wing had one beam, the wing twist was remarkably small, and thus, the aerodynamic forces were nearly the same for the rigid and flexible wings. Notably, for the wing with two beams, the wing twist angle was slightly larger, and the aerodynamic load slightly increased after deformation compared with the wing with one beam. However, the bending of the wing with two beams was smaller than that of the wing with one beam, which resulted in smaller stresses. Therefore, the wing with two beams had a higher strength than the wing with one beam.

The elastic deformation of wings is extremely common. The arrangement of additional beams inside a wing increases the strength of the wing and stabilizes aerodynamic loads but also increases the weight of the wing and the manufacturing cost. Therefore, to select the appropriate wing in real situations, the strength of the wing, wing load, and wing fabrication cost need to be considered in wing design.

A comparison of the total lift coefficient at $M_\infty = 0.3$ in Fig. 17 with the results in Fig. 10 at $M_\infty = 0.6$ shows that the lift coefficient in the first case was substantially smaller than that in the second case. However, in the first case with $M_\infty = 0.3$, the strength of the wing was maintained when the wing was subjected to long-term aerodynamic loads. To increase speed while maintaining an aerodynamic shape, a durable structural solution, such as the arrangement of beams inside the wing, is

necessary. Aerodynamic and structural compromises should also be set to match the technological and financial capabilities.

## 5. Conclusions

Our findings show that aerodynamic force is altered from the aerodynamic design of rigid wings due to elastic wing deformation. These alterations are inevitable. Therefore, the level of wing deformation and the variation in aerodynamic load due to wing deformation must be determined.

The assessments in the current study are a novel implementation of the algorithm coupling the aeroelastic problem from the built aerodynamic code for 3D wings, which considers wing thickness and the built elastic code for 3D hollow wings with beams allocated inside. Within certain definitions of research, these codes allow reductions in running time and memory capacity requirement, the possibility to change the grid automatically, and the convenience of changing the input parameters in selecting the optimal solution. The results of the assessments indicate potentially remarkable changes of the aerodynamic load on the wing when the effect of elastic deformation is considered. Although the aerodynamic force depends solely on the external shape of the wing, structural options need to be accounted for in an attempt to ensure wing durability and predict the aerodynamic load accurately when considering the elastic deformation effect.

## References

[1] N. Yoon, C. Chung, Y. Na and S. Shin, Control reversal and torsional divergence analysis for a high-aspect-ratio wing, *Journal of Mechanical Science and Technology*, 26 (12) (2012) 3921-3931.

[2] D. O. Yu, H. M. Lee and O. J. Kwon, Aerodynamic shape optimization of wind turbine rotor blades considering aeroelastic deformation effect, *Journal of Mechanical Science and Technology*, 30 (2) (2016) 705-718.

[3] A. Varello, A. Lamberti and E. Carrera, Static aeroelastic response of wing-structures accounting for in plane cross-section deformation, *International Journal of Aeronautical and Space Sciences,* 14 (4) (2013) 310-323.

[4] W. Su, S. S. Swei and G. G. Zhu, Optimum wing shape of highly flexible morphing aircraft for improved flight performance, *Journal of Aircraft*, 53 (5) (2016) 1305-1316.

[5] M. H. Nguyen, T. B. N. Hoang and H. S. Nguyen, Calculating aerodynamic characteristics of swept-back wings, *Proceeding of the 14th Asia Congress of Fluid Mechanics*, Vietnam (2013) 132-137.

[6] S. R. Yuvaraj and P. Subramanyam, Design and analysis of wing of an ultralight aircraft, *International Journal of Innovative Research in Science, Engineering and Technology,* 4 (8) (2015) 7456-7468.

[7] N. Goud, G. S. Sathyanarayana, S. S. Babu and T. B. S. Rao, Dynamic aero elastic (flutter) instability characteristics of an aircraft wing, *International Journal of Engineering and Innovative Technology,* 4 (12) (2015) 114-120.

[8] M. Nikbay, L. Oncu and A. Aysan, Multidisciplinary code coupling for analysis and optimization of aeroelastic systems, *Journal of Aircraft*, 46 (6) (2009) 1938-1944.

[9] E. Baskut and A. Akgul, Development of a coupling procedure for static aeroelastic analyses, *Scientific Technical Review*, 61 (3-4) (2011) 39-48.

[10] G. Yang, D. Chen and K. Cui, Response surface technique for static aeroelastic optimization on a high-aspect-ratio wing, *Journal of Aircraft,* 46 (4) (2009) 1444-1450.

[11] J. S. Bae, T. M. Seigler and D. Inman, Aerodynamic and static aeroelastic characteristics of a variable-span morphing wing, *Journal of Aircraft*, 42 (2) (2005) 528-534.

[12] J. Katz and A. Plotkin, *Low speed aerodynamics*, McGraw-Hill, International Edition (1991).

[13] H. S. Nguyen, T. B. N. Hoang, V. P. Dinh and M. H. Nguyen, Experiments and numerical calculation to determine aerodynamic characteristics of flows around 3D wings, *Vietnam Journal of Mechanics,* 36 (2) (2014) 133-143.

[14] T. B. N. Hoang and M. H. Nguyen, Calculation of transonic flows around profiles with blunt and angled leading edges, *Vietnam Journal of Mechanics,* 38 (1) (2016) 1-13.

[15] R. M. Pinkerton, Calculated and measured pressure distributions over the midspan section of the NACA 4412 airfoil, *NASA Technical Reports 563* (1936) 365-380.

[16] T. H. G. Megson, *Aircraft structures for engineering students*, Fourth Ed., Butterworth-Heinemann Publications, Great Britain (2007).

[17] Y. Liu, Efficient methods for structural analysis of built-up wings, *Doctoral Thesis*, University of Virginia, USA (2000).

[18] B. Dupen, *Applied strength of materials for engineering technology,* Indiana University Publications, USA (2014).

[19] American Institute of Steel Construction - AISC, *Specification for structural steel buildings*, USA (2016).

**Hoang Thi Bich Ngoc** is an Associate Professor at the School of Transportation Engineering, HUST, Vietnam, and acquired her M.A. and Ph.D. degrees in France. Fields of her interest include aerodynamics, aeroelasticity, flight mechanics, turbo-machines, and computational calculations.